EFFECTS OF PERTURBATIONS INDUCED BY FRACTURED STENT ON SECONDARY FLOW STRUCTURES IN A CURVED ARTERY MODEL

Kartik V. Bulusu, Christopher Popma and Michael W. Plesniak
Department of Mechanical and Aerospace Engineering
The George Washington University
801 22nd Street, N.W., Washington, D.C. 20052
email: plesniak@gwu.edu

ABSTRACT

Arterial secondary flow structures are affected by pulsatility and multiple harmonics of physiological inflow conditions, resulting in multi-scale vortical patterns. Flow perturbations are produced by stent implants that are used as a treatment to atherosclerosis, a disease of the artery. These perturbations emanate from the Stokes' layer, due to changes in the inner wall surface roughness. The incidence of fractures in stent implants and concomitant flow perturbations result in secondary flow structures with complex, multi-scale morphologies and varying size-strength characteristics. These secondary flow structures are ultimately known to influence wall shear stress and exposure time of blood-borne particles that are closely related to atherogenesis, especially in arterial curvatures. *In vitro* experimental investigation of the complex secondary flow structures due to stent fractures is presented in this study. Particle image velocimetry (2C-2D PIV) techniques are used in conjunction with continuous wavelet transform (CWT) and λ_{ci}-criterion for coherent structure detection. A comparison is made between unfractured and a certain "Type-IV" fracture stent models. The role of centrifugal forces towards the location, translation and breakdown in symmetry of secondary flow structures is explained using a "residual force" parameter.

INTRODUCTION

A common treatment for atherosclerosis is the opening of narrowed arteries resulting from obstructive lesions by angioplasty and stent implantation to restore unrestricted blood flow. One potential complication of this treatment is the incidence of stent fractures that arise due to their structural rigidity and dynamic loading under physiological inflow conditions and vessel tortuosity. There has been an increasing interest of blood flow associated with fractured-stents due the clinical complications such as restenosis and progression of atherosclerosis.

Stent fractures (SFs) may be associated with unanticipated late complications, including clinical in-stent restenosis (ISR), stent thrombosis, and aneurysm formation (Popma *et al.*, 2009; Kim *et al.*, 2009; Adlakha *et al.*, 2010; Alexopoulos & Xanthopoulou, 2011; Nair & Quadros, 2011). There is compelling evidence that links ISR with SFs (Nair & Quadros, 2011; Surmely *et al.*, 2006; Lee *et al.*, 2007; Makaryus *et al.*, 2007). Stent strut fracture-induced restenosis has been reported by Surmely *et al.* (2006) and Makaryus *et al.* (2007). SFs are also considered as a cause of stent reocclusion (or the growth of scar tissue at the sites where the stent damages the arterial wall), where there would be a strong tendency for clots to form (Higashiura *et al.*, 2008; Alexopoulos & Xanthopoulou, 2011). Lee *et al.* (2007) reported adverse clinical outcomes associated with SFs in patients such as restinosis and stent thrombosis. Despite numerous documented occurances of stent fractures there was lack of a uniform method for the detection of SF, grading methodology for their reporting, or time point for their assessment. Jaff *et al.* (2007) addressed the need to define adequate reporting parameters for assessment of metallic stents used in clinical trials of superficial femoral artery atherosclerosis. They categorzied SFs into various failure "Types I-to-V" using a grading system. "Type-IV" SF has been defined therein as a complete transverse, linear fracture of stent struts along with displacement of the stent fragments. Popma *et al.* (2009) presented excellent angiographic evidence of fracture Types II-to-IV and noted a high incidence percentage of angiographic restinosis associated with Type IV fracture (7 out of 18 patients). Krasuski *et al.* (2011) recognized that endothelial effects downstream of stents were central to the development and progression of atherosclerotic plaque. Their study suggested that patients receiving drug-eluting stents (DESs) appeared less likely to develop downstream stenoses than bare metal stents (BMSs).

The mechanisms on how antiproliferatives inhibit the development of downstream coronary lesions remain uncertain. The motivation for the study presented in this paper is derived from the aforementioned open question on development of downstream lesions as a consequence of stents and SFs. The study presented in this paper hypothesizes that secondary flow structures continue to influence the endothelial wall shear stress and create pro-atherogenic conditions downstream of stent implants and SFs. In order to fully understand the effects of secondary flow structures towards the development of restinosis associated with stent implants, the richness in flow physics pertaining to secondary flow structures and disturbances produced by surface roughness of stents and protuberances due to stent fractures need to be examined carefully. Accordingly, the central objective of the study presented herein, is to quantify the spatio-temporal occurances and size-strength characteristics of the complex secondary flow structures under dis-

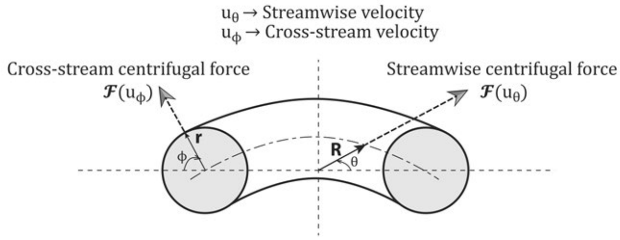

Figure 1. Centrifugal forces acting on fluid flowing in a curved tube

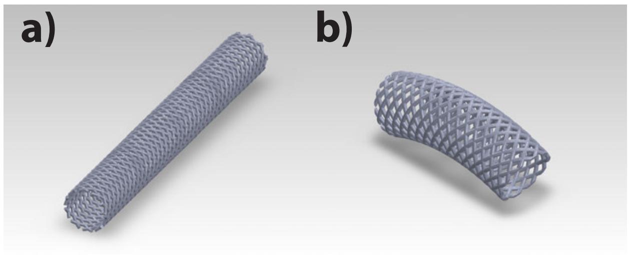

Figure 2. CAD models of stents a) Straight b) Curved

turbed flow downstream of model-stents with and without an idealized Type IV fracture.

Centrifugal forces due to curvature in geometry and pressure gradients under pulsatile inflow conditions produce transitional secondary flow structures. The formation of Lyne vortices in addition to Dean vortices occurs due to the imbalance in the centrifugal forces and pressure gradients (Dean, 1927; Lyne, 1970). Boiron *et al.* (2007), Glenn (2011), Glenn *et al.* (2012) and Bulusu & Plesniak (2013)reported that multiple secondary flow vortex pairs emerge at the 90-degree location in a curved artery test section. Glenn *et al.* (2012) and Bulusu & Plesniak (2013) also observed the presence of smaller scale structures under perturbations induced by a stent-like model that changed the internal diameter of the arterial test section and classified such occurances via a regime map. Webster & Humphrey (1997) describe the following two types of centrifugal forces in a helical coil while presenting the Navier-Stokes equations in toroidal coordinates; (i) streamwise ($u_\theta^2 cos\phi/\xi$) and (ii) cross-stream centrifugal forces (u_ϕ^2/r). These forces emerge due to curvatures in the streamwise and the planar cross-sectional directions respectively and affect the motion and stability of secondary flow structures.

The effect of streamwise and cross-stream centrifugal forces under pulsatile (physiological) flow conditions towards the occurance of multi-scale, multi-strength secondary flow structures is explored in the present study. Accordingly, a new parameter is introduced that describes the effect of centrifugal forces on the location, translation and breakdown in symmetry secondary flow structures. A "residual force" parameter (Equation 1) is the difference between the magnitudes of streamwise and cross-stream centrifugal forces in the curved artery test section.

$$\mathscr{F}_{res} = \frac{u_\theta^2 cos\phi}{\xi} - \frac{u_\phi^2}{r} \tag{1}$$

where $\xi = R + rcos\phi$, R is the radius of curvature of the curved artery test section, r is the radius of the tube cross-section, and ϕ is the angle subtended by a positional vector along the radius r as shown in Figure 1.

EXPERIMENTAL ARRANGEMENT

In vitro experimental investigation of secondary flow structures was performed downstream of model stents that (i) embodied an idealized "Type-IV" SF and (ii) an unfractured configuration within a curved artery test section. The fractured stent fragments were separated by a distance of three blood vessel diameters, where one fragment was located in the curved artery of test section and the other fragment was upstream to the bend. A combination of a straight stent- and a curved stent-section (see CAD models in Figure 2 a,b) embody an idealized "Type-IV" fracture as shown in Figure 3b. Stent models of 88.9 *mm* length and 0.85 *mm* strut diameter were manufactured using a rapid prototyping machine and inserted usptream to the measurement location in the test section (Figure 3 b). The strut thickness of 0.85 *mm* is larger than stents generally implanted in carotid arteries, but embodies an implanted stent with an overgrowth of endothelial cells, producing a corrugated arterial wall.

Two-component, two-dimensional particle image velocimetry (2C-2D PIV) technique was used to acquire phase-locked velocity measurements in a 180-degree curved tube model that is representative of a curved artery (Figure 3). *In vitro* experiments generated secondary flow structures with inflow conditions based on a carotid artery physiological waveform. The experimental set up was fabricated using acrylic (refractive index ≈ 1.45) pipes (12.7 *mm* diameter, 1.2 *m* and 1 *m* lengths) attached to the inlet and outlet to the test section. Flow field illumination was provided by an Nd:YAG laser (532 *nm*, dual pulse) and a CCD camera (LaVision Imager Intense 10Hz) was used as the recording medium. Pulse delay (Δt) was optimized between $600 - 3200 \mu s$ depending on the phase of the cardiac cycle in the driving waveform by checking 8-pixel transition of seed particles at different instances of time. A summary of pertinent PIV recording parameters are presented in Table 1. A programmable gear pump (Ismatec model BVP-Z) was used to provide the inflow (flow rate) and controlled using a customized LabView virtual instrument and data acquisition card (NI DAQ Card-6024E). The PIV system was externally triggered by the programmable pump-instrument control module such that phase-locked measurements could be made at discrete temporal increments on the inflow waveform.

Physiological waveform

The physiological carotid artery waveform was reconstructed from ultrasonic flowmeter measurements on the left carotid artery reported by Holdsworth *et al.* (1999). This waveform was discretized to 100 evenly-spaced instants (in time) spanning a period (T) of 4 seconds. The time interval between discretized points was 40×10^{-3} seconds. The physiological waveform is the superposition of multiple harmonic frqeuncies and therefore, each harmonic can be associated with a unique Womersley (W_o), mean Reynolds (Re_{avg}) and a mean Dean number (De_{avg}). For one complete period of the waveform ($T = 4$ s) and a tube inner diameter of 12.7 *mm* (Figure 4) , the waveform will possess only a single Womersley number ($W_o = 4.2$), one mean Reynolds number ($Re_{avg} = 383$) and one mean Dean num-

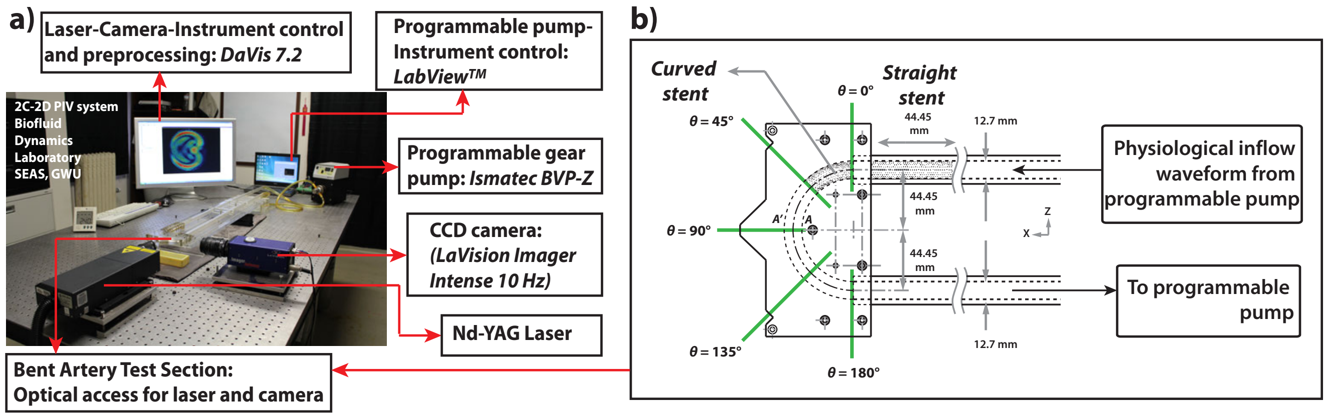

Figure 3. Experimental set-up a) 180^o curved tube model for curved arteries b) CAD Model of stent installed at the specified location

Table 1. PIV recording parameters for secondary flows in the 180^o curved tube

Flow geometry	Circular cross-section parallel to light sheet
CCD Array (pixels)	x 1376, y 1040
Final number of vectors	x 86, y 65
Pulse delay	$\Delta t = 600 - 3200\mu s$
Seeding material	Flouro-Max Red^{TM} fluorescent polymer microspheres
Seeding particle diameter (d_p)	$\approx 7\mu m$
Dynamic spatial range (DSR)	32:1
Dynamic velocity range (DVR) (at $t/T = 0.21$; see Figure 4)	50.6:1

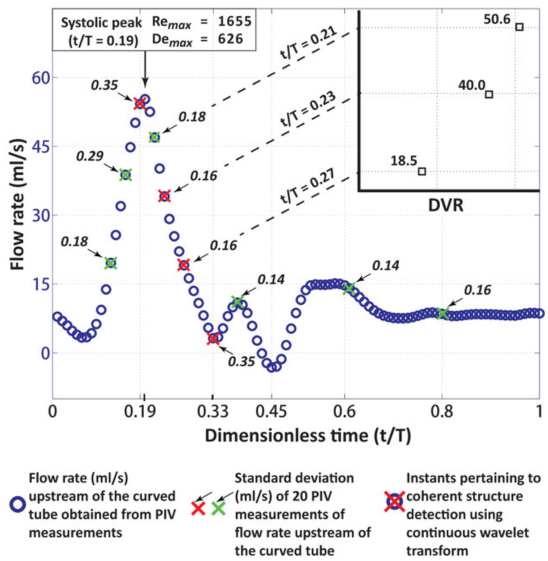

Figure 4. Carotid artery waveform

ber ($De_{avg} = 145$). Flow rate presented in Figure 4 was calculated by integrating the velocity profiles across the inner diameter of the tube, upstream of the bend. The flow rate cycle-to-cycle variations were minimal with excellent confidence levels as evidenced by standard deviations (less that 2%) at various instances shown in Figure 4. Optical access to the fluid for planar velocity measurements necessitated that the blood-analog fluid have a refractive index closely matched with the optical test rig. All the experiments were performed at the controlled room temperature of $24^oC(\pm 1^o)$. A summary of the hydrodynamic experimental parameters is presented in Table 2.

PIV data ensembles

Post-processing of phase-locked data ensembles involved the calculation of phase-averaged and root-mean-squared (RMS) velocity, and phase-averaged vorticiy (ω). Adrian (1997) states that large dynamic spatial (DSR) and dynamic velocity range (DVR) values are desireable for the estimation of large-scale coherent structures. DVR varies under pulsatile flow scenarios and is reported at few points (see Figure 4 and Table 1). A total of 100 PIV data ensembles (one ensemble per instance in the physiological waveform) were generated at a chosen location in the bend. Each data ensemble was comprised of 200 PIV realizations, for statistical convergence of velocity (1-3% of stationary values) at the chosen (90-deg) cross-section in the bend. The number of PIV realizations in each ensemble was therefore, sufficiently large with acceptable confidence levels. 100 phase-averaged vorticity fields were generated, one for each discrete (time) point on the physiological waveform shown in Figure 4.

COHERENT STRUCTURE DETECTION AND ANALYSIS

Secondary flow structures are conceptually modeled as swirling vortical structures that are either rotation-dominated or strain-dominated. We treated secondary flow structure phenomena as multi-scale and multi-strength occurrences. During the course of the experiments, transitional secondary flow structures were observed exclusively at the 90-deg location and necessitated size-structure and strength considerations (via wavelets) to be resolved accurately. Continuous wavelet transform (CWT) was implemented using a Ricker wavelet (as the mother wavelet, ψ) to characterize the shape of two-dimensional vortical patterns. Following Farge *et al.* (1990), Kailas & Narasimha

Table 2. Experimental parameters pertaining to the physiological waveform with the blood-analog fluid

Blood-analog fluid (reported by Deutsch *et al.* (2006))	79% saturated NaI, 20% pure glycerol, and 1% water (by volume)
Kinematic viscosity (ν)	3.55 cSt ($\pm$2.8%)
(using a standard Ubbelhode viscometer at 25^oC)	$3.55\times10^{-6}m^2/s$
Refractive index(Atago PAL-RI refractometer)	1.45 ($\pm$3.4%)
Maximum Dean number (De_{max})	626
Maximum Reynolds number (Re_{max}) (at $t/T=0.19$; see Figure 4)	1655
Average Dean number (De_{avg})	145
Average Reynolds number (Re_{avg})	383
Period of the waveform (T)	4 *seconds*
Womersley number (W_o)	4.2
Duration of systolic deceleration ($0.19\leq t/T\leq 0.33$; see Figure 4)	560×10^{-3} s

(1999) and Schram & Riethmuller (2001), guidelines on the choice of the mother wavelet (ψ) and the restrictions thereof, are noted herein as (i) preservation of the L^2 norm, (ii) admissibility and (iii) good localization and smoothness both in physical and spectral spaces. Furthermore, Kailas & Narasimha (1999), Schram & Riethmuller (2001) and Varun *et al.* (2008), note the suitability of the 2D Ricker wavelet (as represented by equation 2) toward educing vortical patterns of interest.

$$\psi(x,y)=\{2-(\frac{x}{\sqrt{\ell}})^2-(\frac{y}{\sqrt{\ell\varepsilon}})^2\}\,exp\{-(\frac{(\frac{x}{\sqrt{\ell}})^2+(\frac{y}{\sqrt{\ell\varepsilon}})^2}{2})\} \quad (2)$$

where ℓ is the scale factor and ε controls the wavelet isotropy. PIV-generated measurement ensembles (or images) of vorticity (ω) are treated as the untransformed original signals. CWT is applied using a 2D Ricker wavelet to generate *transformed signals*, or wavelet transformed vorticity fields ($\tilde{\omega}$). The 2D Ricker (or any) wavelet is scaled infinitely, such that CWT at each scale represents an exhaustive pattern search for secondary flow structures; a computationally expensive process. Therefore, an *optimal wavelet scale* is defined as that where coefficients of the *transformed signal* most efficiently represent the *original signal*. We developed an alogrithm (PIVlet 1.2) that performs wavelet transforms on vorticity data and computes Shannon entropy of the wavelet transformed vorticity ($\tilde{\omega}$) toward an optimal wavelet scale and the resolution of multi-scale secondary flow structures (Bulusu & Plesniak, 2013).

In addition, the velocity gradeint tensor is computed for each pixel (of $M\times N$ array of pixels) in 2D-PIV generated (images or) data using a first order central difference scheme. Resulting eigen values of 2×2 matrices at each pixel were of the form, $\lambda_{cr}\pm i\lambda_{ci}$. Iso-$\lambda_{ci}$-regions where $\lambda_{ci}>0$ represent vortices (Adrian *et al.*, 2000). For 2C-2D PIV measurements, the axes of vortical rotation are not always perpendicular to the place of measurements and hence, off-axes vortical patterns are not clearly resolved. But for the study presented herein, the λ_{ci} - criterion serves two purposes; (i) in providing a physical means of vortical pattern detection and, (ii) and validation of the multi-scale vortical patterns observed in $\tilde{\omega}$-fields.

RESULTS

The systolic deceleration phase of the cardiac cycle produced a variety of secondary flow structures, possessing distinct size-strength configurations as evidenced in previous studies by Bulusu & Plesniak (2013), Glenn *et al.* (2012), Boiron *et al.* (2007) and Sudo *et al.* (1992). The secondary flow structures are labelled as deformed-Dean-, Lyne- and Wall-type vortices (D-, L- and W-type) and were in agreement with similar observations by Bulusu & Plesniak (2013), Sudo *et al.* (1992) and Glenn *et al.* (2012) in size-strength characteristics at the 90-deg location. Accordingly, physiological flow measurements with the unfractured stent and the idealized Type IV stent fracture model were made at the 90^o planar location during the systolic deceleration (t/T = 0.18, 0.23, 0.27, 0.33) in the curved artery test section.

Firstly, a comparison between λ_{ci} and $\tilde{\omega}$ within Figures 5 and 6, shows that there is good agreement in the type of flow structures detected. Both λ_{ci} and $\tilde{\omega}$ were implemented without any artifical thresholding in order to demonstrate validity of CWT through visual confirmation of flow structures. Secondly, $\tilde{\omega}$ generated by the CWT-alogrithm produced better resolution of secondary flow morphologies especially, during the late systolic deceleration phase ($t/T>0.23$) compared to unthresholded-λ_{ci}.

Differences in secondary flow morphologies between unfractured and fractured configuration can be observed in direct comparison of Figures 5 and 6. The breakdown in symmetry of D-L-W structures in the unfractured-case, and depletion in strength of D-L-W structures in the idealized Type IV stent fractured-case are clearly detected in the $\tilde{\omega}$-contours. In the unfractured stent-case (Figure 5) a deformed Dean- (D) and Lyne-type (L) configuration was observed at $t/T=0.18$, transforming into a D-L-W configuration at $t/T=0.23$ and progressing towards a breakdown in symmetry at $t/T=0.27$. D-L-W configuration along with the presence of smaller scale Lyne- and Wall-type structures are noticed at the onset of systolic peak in the idealized Type IV stent fracture-case (Figure 6) at $t/T=0.18$. The secondary flow structures in the fractured stent-case are evidenced by (i) an early onset of D-L-W structures at $t/T=0.18$, (ii) no predominant breakdown in structures and (iii) a depletion in strength and shape of the structures during systolic deceleration that persisted until the end of the systolic deceleration phase ($t/T=0.23$ to $t/T=0.33$). Cross-stream and streamwise centrifugal force distributions are presented at $t/T=0.27$ only, focussing exclusively on the phenomenon of breakdown in symmetry (Figure 7). But it is understood that $\mathscr{F}_{res}$ can be computed for PIV data at every instance of time in the physiological waveform. In addition, $\mathscr{F}_{res}$, was computed with the centerline velocity (u_θ) for the streamwise centrifugal force and was sufficient towards understanding the role of the streamwise centrifugal force. A non-uniform $\mathscr{F}(u_\phi)$-distribution was observed at the locations of secondary flow structures suggesting that cross-stream centrifugal forces lead to loss of coherence in vortical structures (see Figure 7, 2nd column). Simi-

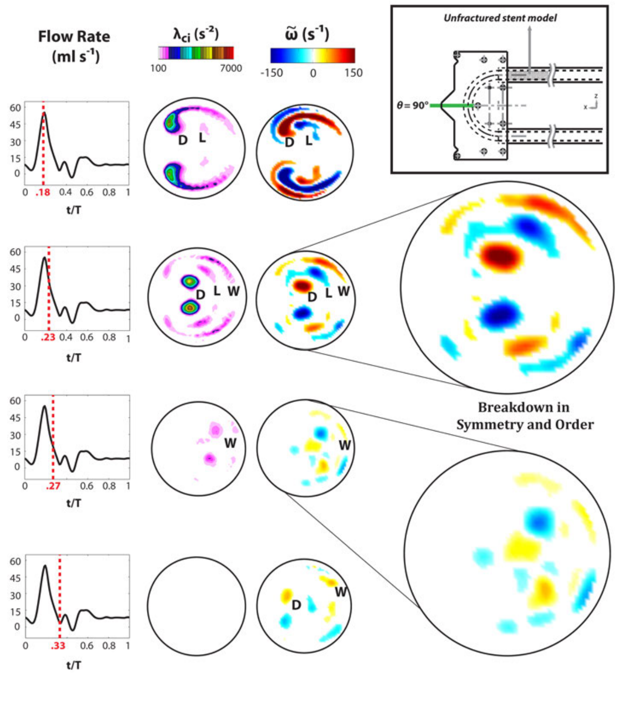

Figure 5. Secondary flow structures with an unfractured stent

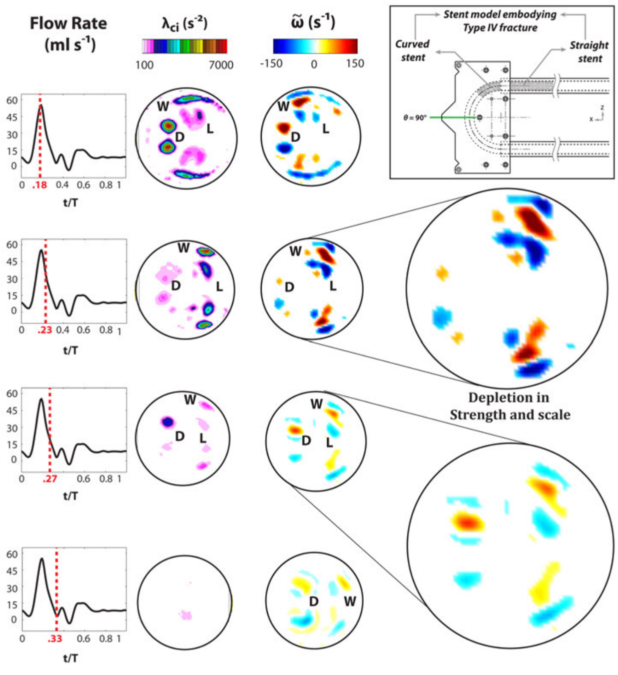

Figure 6. Secondary flow structures with an idealized "Type IV" stent fracture

larly, a non-uniform $\mathscr{F}(u_\phi)$-distribution is observed in the idealized Type-IV stent fracture-case around the deformed Dean-type vortex (D) (see Figure 7, 2nd column). This suggests that secondary flow structures with non-uniform $\mathscr{F}(u_\phi)$-distribution remain susceptible to loss of coherence and large scale changes in size and strength. The wall-type (W) vortices in the fractured stent-case possess a uniform $\mathscr{F}(u_\phi)$-distribution indicating persistance in vortical size and strength.

The streamwise centrifugal forces have a greater magnitude than the cross-stream centrifugal forces and therefore, $\mathscr{F}_{res}$ $(= \mathscr{F}(u_\theta) - \mathscr{F}(u_\phi))$ explains the translation of vortical structures towards the outer wall and confirmed by the location of the low strength vortical structures in the unfractured stent-case and the wall-type vortices (W) in the fractured stent-case. The deformed Dean-type vortex (D) in the fractured stent-case is subjected to the lower $\mathscr{F}_{res}$ and a greater balance between competing forces, $\mathscr{F}(u_\theta)$ and $\mathscr{F}(u_\phi)$. Hence, it located away from the outer wall (see Figure 7, 3rd column). The aforementioned results though location-specific (90-deg plane), can easily be extended to other cross-sectional locations in the curved artery test section. In addition, simultaneous measurements of planar u_θ profiles using stereo-PIV or tomographic-PIV, can significantly improve our understanding of the role of centrifugal forces using $\mathscr{F}_{res}$.

CONCLUSIONS

The overarching goal of the study was to quantify the multi-scale and multi-strength secondary flow structures that were observed in a curved artery test-section under physiological inflow conditions, in the presence of model-stent implants with and without an idealized Type IV fracture. The distribution of centrifugal forces, streamwise $(\mathscr{F}(u_\theta))$ and cross-stream $(\mathscr{F}(u_\phi))$ determine the location, size and the degree of coherence of arterial secondary flow structures. The distribution of the cross-stream centrifugal forces as observed in the contours of $\mathscr{F}(u_\phi)$ suggests that the vortices experiencing a uniform $\mathscr{F}(u_\phi)$ have greater degree of coherence. The residual force parameter, $\mathscr{F}_{res}$, along with the cross-stream centrifugal force, $\mathscr{F}(u_\phi)$ has the potential to explain the loss of coherence and vortical symmetry of arterial secondary flow structures.

REFERENCES

Adlakha, S., Sheikh, M., Wu, J., Burket, M. W., Pandya, U., Colyer, W., Eltawahy, E. & Cooper, C. J. 2010 Stent fracture in the coronary and peripheral arteries. *Journal of Interventional Cardiology.* **23** (4), 411–419.

Adrian, R. J. 1997 Dynamic ranges of velocity and spatial resolution of particle image velocimetry. *Meas. Sci. Technol.* **8**, 1393–1398.

Adrian, R. J., Christensen, K. T. & Liu, Z. C. 2000 Analysis and interpretation of instantaneous turbulent velocity fields. *Experiments in Fluids* **29**, 275–290.

Alexopoulos, D. & Xanthopoulou, I. 2011 Coronary stent fracture: How frequent it is? does it matter? *Hellenic J. Cardiol.* **52**, 1–5.

Boiron, O., Deplano, V. & Pelissier, R. 2007 Experimental and numerical studies on the starting effect on the secondary flow in a bend. *J. Fluid Mech.* **574**, 109–129.

Bulusu, K. V. & Plesniak, M. W. 2013 Secondary flow morphologies due to model stent-induced perturbations in a 180 curved tube during systolic deceleration. *Experiments in Fluids* **54(3)**, 1493.

Dean, W. R. 1927 Note on the motion of a fluid in a curved pipe. *Phil. Mag.* **7**, 208–223.

Deutsch, S., Tarbell, J. M., Manning, K. B., Rosenberg, G. & Fontaine, A. A. 2006 Experimental fluid mechanics of pulsatile artificial blood pumps. *Annu. Rev. Fluid Mech.* **38**, 65–86.

Farge, M., Guezennec, Y., Ho, C. M. & Meneveau, C. 1990 Continuous wavelet analysis of coherent structures. *Cen-*

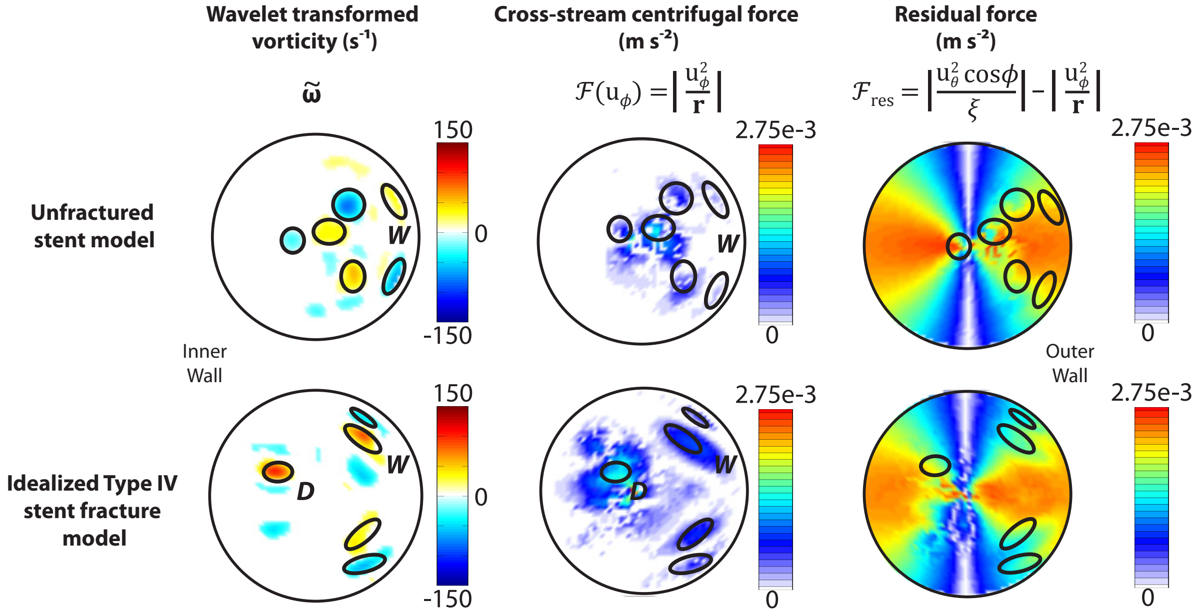

Figure 7. $\tilde{\omega}$, $\mathscr{F}_\phi$ and $\mathscr{F}_{res}$ at $t/T = 0.27$ and 90-degree location in the curved artery test section

ter for Turbulence Research, Proceedings of the Summer Program pp. 331–348.

Glenn, A. L. 2011 Classification of Secondary Vortices in a Curved Pipe Model of an Artery. Master's thesis, The George Washington University, Washington DC.

Glenn, A. L., Bulusu, K. V., Shu, F. & Plesniak, M. W. 2012 Secondary flow strcutures under stent-induced perturbations for cardiovascular flow in a curved artery model. *International Journal of Heat and Fluid Flow* .

Higashiura, W., Sakaguchi, S., Morimoto, K. & Kichikawa, K. 2008 Stent fracture and reocclusion after placement of a single self-expanding stent in the common iliac artery and endovascular treatment. *Cardiovasc. Intervent. Radiol.* **31**, 1013–1017.

Holdsworth, D.W., Norley, C. J., Frayne, R., Steinman, D. A. & Rutt, B. K. 1999 Characterization of common carotid artery blood-flow waveforms in normal human subjects. *Physiol. Meas.* **20(3)**, 219–40.

Jaff, M., Dake, M., Popma, J., Ansel, G. & Yoder, T. 2007 Standardized evaluation and reporting of stent fractures in clinical trials of noncoronary devices. *Catheterization and Cardiovascular Interventions* **70**, 460–462.

Kailas, S. V. & Narasimha, R. 1999 The eduction of structures from flow imagery using wavelets: Part i. the mixing layer. *Experiments in Fluids* **27**, 167–174.

Kim, S. H., Kim, H. J., Han, S. W., Jung, S. M., Kim, J. S., Chee, H. K. & Ryu, K. H. 2009 A fractured sirolimus-eluting stent with a coronary aneurysm. *Ann. Thorac. Surg.* **88**, 664–665.

Krasuski, R. A., Cater, G. M., Devendra, G. P., Wolski, K., Shishehbor, M. H., Nissen, S. E., Oberti, C. & Ellis, S. G. 2011 Downstream coronary effects of drug-eluting stents. *American Heart Journal.* **162** (4), 764–771.

Lee, M. S., Jurewitz, D., Aragon, J., Forrester, J., Makkar, R. R. & Kar, S. 2007 Stent fracture associated with drug-eluting stents: Clinical characteristics and implications. *Catheterization and Cardiovascular Interventions* **69**, 387–394.

Lyne, W. H. 1970 Unsteady flow in a curved pipe. *J. Fluid Mech.* **45**, 13–31.

Makaryus, A. N., Lefkowitz, L. & Lee, A. D. K. 2007 Coronary artery stent fracture. *Int. J. Cardiovasc. Imaging* **23**, 305–309.

Nair, R. N. & Quadros, K. 2011 Coronary stent fracture: A review of the literature. *Cardiac Cath Lab Director.* **1**, 32–38.

Popma, J. J., Tiroch, K., Almonacid, A., Cohen, S., Kandzari, D. E. & Leon, M. B. 2009 A qualitative and quantitative angiographic analysis of stent fracture late following sirolimus-eluting stent implantation. *Am. J. Cardiol.* **103** (7), 923–929.

Schram, C. & Riethmuller, M. L. 2001 Vortex ring evolution in an impulsively started jet using digital particle image velocimetry and continuous wavelet analysis. *Meas. Sci. Technol.* **12**, 1413–1421.

Sudo, K., Sumida, M. & Yamane, R. 1992 Secondary motion of fully developed oscillatory flow in a curved pipe. *J. Fluid Mech.* **237**, 189–208.

Surmely, J. F., Kinoshita, Y., Dash, D., Matsubara, T., Terashima, M., Ehara, M., Ito, T., Nasu, K., Takeda, Y., Tanaka, N., Suzuki, T. & Katoh, O. 2006 Stent strut fracture-induced restenosis in a bifurcation lesion treated with the crush stenting technique. *Circ. J.* **70**, 936–938.

Varun, A. V., Balasubraminian, K. & Sujith, R. I. 2008 An automated vortex detection scheme using the wavelet transform of the d_2 field. *Experiments in Fluids* **45**, 857–868.

Webster, D. R. & Humphrey, J. A. C. 1997 Traveling wave instability in helical coil flow. *Phys. Fluids* **9(2)**, 407–418.